Applied Physics A (2021) 127:641
https://doi.org/10.1007/s00339-021-04781-6

Applied Physics A
Materials Science & Processing

Characterization and application of niobium-doped titanium dioxide thin films prepared by sol–gel process

Gustavo Henrique M. Gomes[1] · Magnum A. M. L. de Jesus[1] · André S. Ferlauto[2] · Marcelo M. Viana[1] · Nelcy D. S. Mohallem[1]

Received: 29 April 2021 / Accepted: 19 July 2021

Abstract

Pure and Nb-doped TiO_2 crystalline thin films with different molar ratios of niobium were produced by sol–gel process using the dip-coating method. The results of X-ray diffractometry analysis using Rietveld refinement confirmed the presence of the anatase phase and the partial substitution of Ti^{4+} by Nb^{5+} in the [TiO_6] octahedra, since changes in the lattice parameters, crystalline strain and crystallite size were observed. The occupation of niobium atoms at the Ti^{4+} sites and an increase in the oxygen content were also determined. Atomic force microscopy analyses showed a uniform and homogeneous surface morphology and high-resolution transmission microscopy showed agglomerated nanoparticles. Nanoindentation and ellipsometry techniques evidenced that the insertion of Nb in the TiO_2 matrix caused an increase in density and hardness (~ 18%) values and a reduction in the root mean square (RMS) values (30 and 75% of reduction for 3% and 1% Nb/TiO_2). Nb-doped TiO_2 thin films showed better performance in the photodegradation of methylene blue, reaching a degradation rate of 44% after 4 h of testing, against 26% for pure TiO_2 thin film. The reaction rate was almost twice as high for the doped thin film, with a half-life time of 285 min versus 529 min for pure TiO_2 film.

✉ Nelcy D. S. Mohallem
nelcy@ufmg.br

[1] Nanostructured Materials Lab, Department of Chemistry, Federal University of Minas Gerais, Av. Antônio Carlos, 6627, Belo Horizonte, Minas Gerais 31270-901, Brazil

[2] Centro de Engenharia, Modelagem e Ciências Sociais Aplicadas, CECS, Federal University of ABC, Av. dos Estados, 5001, Bairro Santa Terezinha, Santo André, SP, Brazil

Published online: 02 August 2021

Graphic abstract

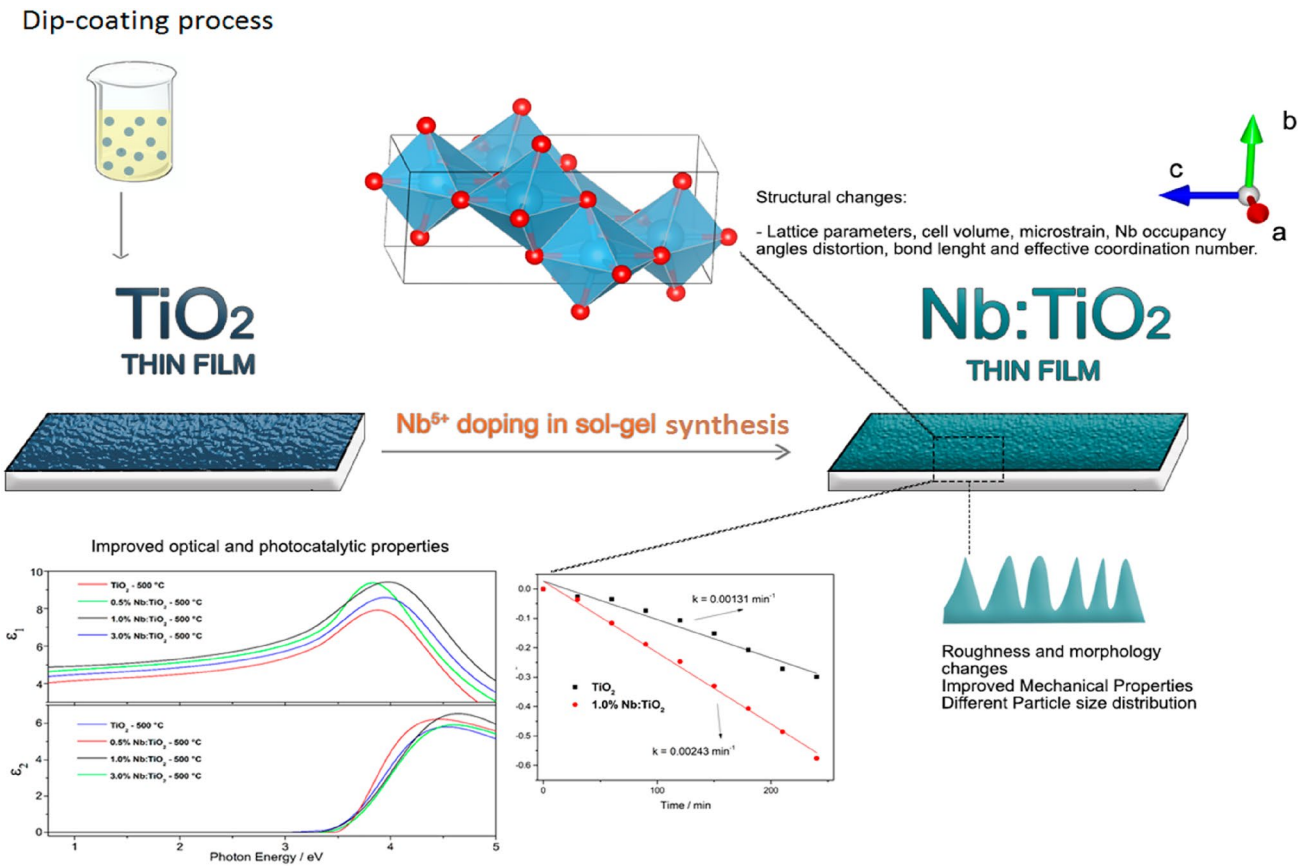

Keywords Nb/TiO_2 thin films · Nb-doped TiO_2 · Photodegradation

1 Introduction

Titanium dioxide thin film is a well-known multifunctional material, broadly studied, whose properties can be modulated through combinations with several other metallic cations, promoting the development of modified materials with different properties and superior performance than pure films [1–4]. Some features of doped TiO_2 thin films that have aroused interest involve modification in structural and electronic properties, such as changes in bandgap values [5, 6], dielectric function [7], photocatalytic activity [8–10] for use in applications such as water disinfection [11, 12], hydrophilic surfaces and as transparent conductive oxides (TCO) [13, 14].

The use of niobium in the production of doped TiO_2 thin films has been studied, due to the substitution defects that occur in their structure, since the Nb^{5+} and Ti^{4+} atoms have analogous chemical nature with similar ionic radii and charges [15]. Some studies have reported changes in bandgap [16, 17], crystalline structure [5] and the improvement of some properties, such as the sensitivity of CO_2 gas sensor [18], lower resistivity in TCO, improved electrical properties [19] and better photocatalytic performance in water treatment [20]. Although there are several studies recently reported, there is a lack of understanding about how Nb alters the optical, mechanical and photocatalytic properties of TiO_2 films, and how these properties are correlated to the niobium content. These studies have showed how the amount of niobium inside the TiO_2 matrix affects its microstructure, pointing to the segregation problem between TiO_2 and Nb_2O_5 with high niobium content [17]. Some reports also demonstrated how different amounts of Nb change the bandgap values and the electrical properties [13, 15, 19].

Nb-doped TiO_2 anatase thin films have been deposited by several methods, such as radio-frequency magnetron co-sputtering [21], atomic layer deposition [14], chemical vapor deposition [22] and sol–gel process [18, 23–25]. Despite the number of publications on several synthetic methods, sol–gel process showed to be efficient due to its simplicity, reproductibility, being a simple and low-cost process, allowing to

control the microstructure by changing the reaction kinetics and deposition parameters. This process also presents features such as good control of thickness and porosity, homogeneous surface, reproducibility, mild reactions conditions and good control of stoichiometry including nanocomposite systems or doped thin films [26–28]. Manole et al. [29] evaluated changes in the structural and optical properties of Nb-doped TiO_2 thin films by spectroscopic ellipsometry, using the "new amorphous" dispersion formula as an analytical function to model data from adequate parameters for amorphous films. Rasheed et al. [30] determined the optical constants of ITO, TiO_2 and TiO_2/Nb ultrathin films on glass and PET substrates by spectroscopic ellipsometry and spectrophotometry, also using the "new amorphous model". Despite all the reports in the literature, none has been found on Nb doping in TiO_2 films obtained by controlled sol–gel method and dip-coating process, employing ammonium niobium oxalate as precursor and correlating the ellipsometric parameters (dielectric function (ε), thickness, roughness and optical bandgap) with a detailed structural and mechanical characterization (XRD, Rietveld refinement, HRTEM and AFM nanoindentation).

This work aims to study the influence of Nb doping in the thin film of TiO_2 anatase, prepared by a low-cost sol–gel process, and its optical and mechanical properties. The optical properties were evaluated by UV–Vis spectroscopy and spectroscopy ellipsometry applying the Tauc–Lorentz oscillator, with CompleteEASE software, adequate for nanocrystalline thin films, and the mechanical (nanohardness measurements) properties by nanoindentation. The changes in the Nb/TiO2 microstructure were evaluated, and the photocatalytic activity against methylene blue dye pollutant was also studied.

2 Materials and methods

2.1 Sol–gel synthesis and thin film deposition

TiO_2 solution was prepared using titanium isopropoxide (TTIP—$Ti(OCH(CH_3)_2)_4$—97% Sigma-Aldrich), isopropyl alcohol (99.5%, NEON), glacial acetic acid (99% Synth), hydrochloric acid (37 wt% m/m, Synth) and acetylacetone (99%, Merck), with a molar proportion of 2.2/115/1/11.3/1.9, respectively, as previously reported [27]. Ammonium niobium oxalate ($NH_4[NbO(H_2O)0.2](H_2O)_2$) was provided by Companhia Brasileira de Metalurgia e Mineração (CBMM) and was used as niobium precursor. An acidic solution (HNO_3—concentration of 0.001 mol.L^{-1}) of the inorganic complex was prepared at pH = 3 and added dropwise in the previous TiO_2 solution until the desired Nb/Ti molar ratio of $Nb_xTi_{1-x}O_2$, where $x = 0$, 0.005, 0.01 or 0.03).

First, we added the isopropyl alcohol inside a beaker at constant stirring with the acid content to prevent TiO_2 precipitation. After the solution homogenization, the TTIP has been added dropwise with the acetylacetone. Thin films were deposited on soda lime glasses using the dip-coating method employing a calibrated equipment specially designed for our purpose. The substrates were previously cleaned for 10 min on ultrasound bath with distilled water and alkaline soap, washed vigorously with distilled water and then washed with isopropyl alcohol for 15 min in ultrasound bath. The thin films were deposited on the substrates at constant withdrawal speed (0.120 cm·s^{-1}) and annealed at 400 and 500 °C for one hour in air atmosphere. The process was repeated 5 times to achieve the desired thickness and carried out this way to avoid sodium diffusion from the soda lime glass substrate to the thin film, as reported in the literature [31].

2.2 Characterization of thin films

Morphology and texture of the films were evaluated by transmission electron microscopy (TEM—Tecnai G2-20—SuperTwin FEI—200 kV) and scanning probe microscopy (SPM—AFM—MFP-3D-SA ASYLUM RESEARCH) in intermittent contact mode. The mechanical properties measurements (nanohardness and Young modulus) were performed using a nanoindenter attached to the SPM head, according to ISO 14,577. The measurements were made using a Berkovich tip and a controlled load method. Five-layer films were placed directly on the sample holder to eliminate the influence of the substrate in the measurements. The indentation area was 50 µm × 50 µm with 36 measurement points analyzed [18]. The Young's modulus and nanohardness were calculated from the discharge portion of indentation curves using the method of Oliver & Pharr [32].

The crystal structure of the thin films was evaluated using X-ray diffraction (XRD, Shimadzu XRD-7000) with Cu radiation, angle 0.9°, step scan of 0.02° and acquiring data time of 3 s, in the range of 15–70°. Rietveld refinement was performed using the GSAS-EXPGUI software. The crystallite size and strain measurements employed the Lorentzian part of the profile function (LX and LY) that accounts for the full width at half-maximum (FWHM) of the peaks. The UV–Vis spectroscopy results were used to determine the optical bandgap of the thin films by the traditional Tauc method [33].

Spectroscopic ellipsometry (SE—M-2000 from J.A. Woollam Company) was used to detect changes in the psi (Ψ) and delta (Δ) parameters. The dielectric function (ε), thickness, roughness and optical bandgap (Eg) were determined by analyzing the Ψ and Δ data (0.5–5.0 eV) using the CompleteEASE software. The psi (Ψ) and delta (Δ) describe the change in polarization that occurs when the light beam interacts with the sample surface. The incident light beam

has electric fields, parallel (*p*-) and perpendicular (*s*-) to the plane of incidence, and psi (Ψ) and delta (Δ) represent the amplitude ratio and phase difference between *p*- and s- polarization directions, respectively [34]. The relation between Ψ and Δ is

$$\rho \equiv \tan \Psi e^{(i\Delta)} \equiv \frac{r_p}{r_s}, \quad (1)$$

where ρ is the total polarization, tan Ψ represents the amplitude change, Δ represents the phase change and r_p and r_s are the Fresnel reflection coefficients for the *p*- and *s*-polarized light. Ψ and Δ hold information about the studied material, and using the proper mathematical model, it is possible to obtain information about the thickness, bandgap, roughness, refractive index and extinction coefficient. Ellipsometry analysis was adjusted by a least square regression analysis using Cauchy and Tauc–Lorentz analytical functions. The porosity of thin films was evaluated using the Lorentz–Lorenz model. The methodology and mathematical models used to obtain the parameters related to ellipsometry and porosity are described elsewhere [27].

2.3 Photocatalytic tests

The photocatalytic activities of doped and undoped titanium dioxide thin films were carried using a Phillips UV-C lamp, with 15 W, UVC output of 4.9 W at wavelength of 253 nm, inside an UV chamber. Methylene blue was used as a model for dye or pollutant inside water solutions, and its starting concentration in solution was 10 ppm. The thin film samples with dimensions of 1 × 5 cm were placed inside open falcon tubes with the methylene blue solution distant of 20 cm from the UV-C lamp, with an approximated irradiance of 2.6 W/m^2. The test was carried for one hour in the dark to ensure the adsorption equilibrium, and then, every thirty minutes an aliquot was collected to perform the analysis by ultraviolet–visible spectroscopy (UV–Vis) in the range of 500–750 nm, with maximum absorption of methylene blue at 663 nm, until complete 4 h of photocatalytic tests.

3 Results and discussion

3.1 Structural, morphological and mechanical characterization of thin films

The XRD measurements show the presence of anatase titanium dioxide phase in all annealed samples at 500 °C (PDF # 21–1272), as seen in Fig. 1a. The anatase phase has a tetragonal crystalline system with space group I41/amd (No. 141), which consists of a unit cell with $a = b \neq c$ with all axis being orthogonal between then ($\alpha = \beta = \gamma = 90°$) [15, 19]. The peaks corresponding to crystalline planes (004)—38.12°, (105)—54.34°, (211)—55.30°, (204)—63.11°, (116)—69.33°, (220)—70.56°, and (215)—75.55°, are masking others of anatase phase, due to a peak broadening caused by the small crystallite size and strains in the crystal structure. The peaks related to Nb/TiO_2 showed a displacement, which can be seen in Fig. 1b, where the peak of the

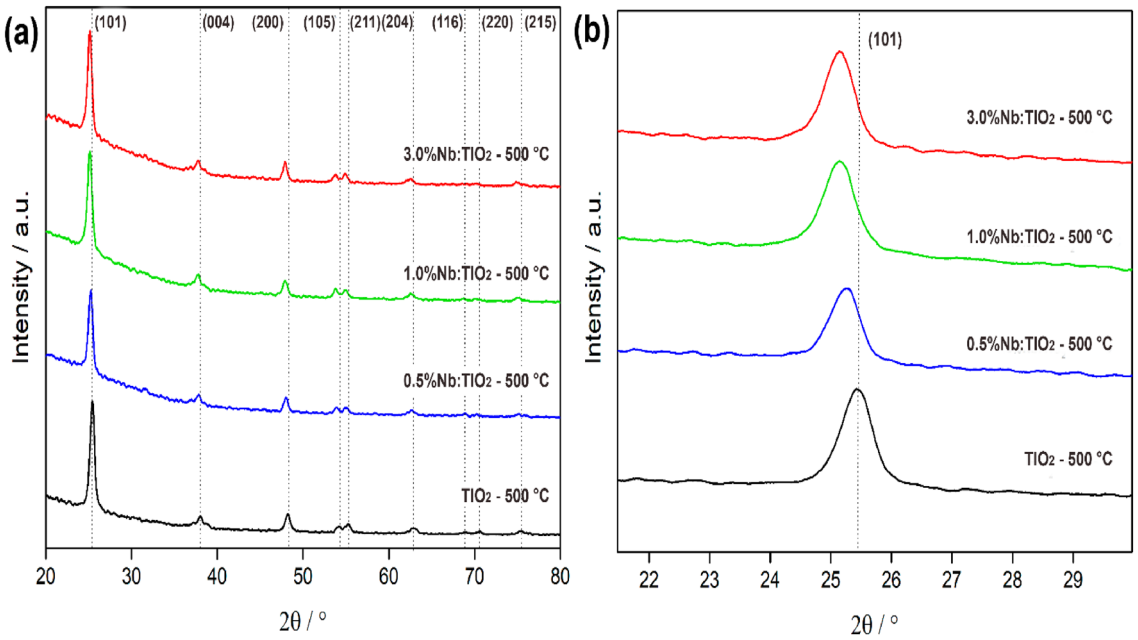

Fig. 1 XRD patterns of doped and undoped TiO_2 thin films **a** calcined at 500 °C and **b** magnification at (101) crystal plane of anatase

non-doped TiO_2 was taken as reference. This phenomenon is correlated to the niobium insertion inside the TiO_2 matrix, since niobium and titanium atoms have different radii and charges, provoking a distortion, which change the values of lattice parameters and cell volumes. This behavior is also characteristic of an increase of the strain in the sample. This supports the hypothesis that niobium atoms are incorporated into the anatase TiO_2 lattice and do not segregate in a separate phase [15, 19].

Rietveld refinement was performed to obtain crystal data of the samples. The first order Shifted polynomial Chebyshev function, defined as

$$T_n^*(x) = T_n(2x - 1) \tag{2}$$

with $x \in [0,1]$, where $T(x)$ is the polynomial function and n is its degree, was used to fit the background using $n = 12$. The refined parameters in all samples are the zero drift, scale factor, profile function with FWHM, strain and crystallite size broadening, peak asymmetry, spherical preferential orientation, unit cell parameters, atomic coordinates and occupancy. The obtained values of χ^2, which depends on *R*wp/% (weighted profile *R*-factor) and *R*p/% (profile *R*-factor), indicate a good fit to all samples (Table 1), since a good refinement of thin films is hard to obtain. RF/% (structure factor), which measures the agreement between the calculated and experimental peak intensity, demonstrated good coherence with the standard crystallographic information file (CIF). The *R* parameters represent the discrepancy between the calculated and observed intensities in each point of the diffractogram and a low value of the sum provides reliability on the analysis results [35]. The $X^2 = 1$ means the best possible fit of the parameters and $X^2 < 1.35$, which was obtained in all analysis, represent good correlation between the obtained data and the calculated model.

Figure 2 shows the obtained graphs from Rietveld analysis. The blue curve appears almost flat in all refinements, also indicating a good fitness of the samples. Table 2 presents the obtained data from Rietveld refinement. The addition of niobium inside the TiO_2 matrix promotes an increase in the lattice parameters, which can be attributed to the fact that the cation radius of Nb^{5+} (0.064 nm) is larger than that of Ti^{4+} (0.061 nm) [19]. Kamisaka et al. [15] reported that the presence of niobium causes some distortions in the crystalline network, showing an increase of 0.517% for "a" and "b" lattice parameters, which corroborates with the obtained data, showing an increase of 0.48% for the 0.5%Nb/ TiO_2. The niobium addition provokes an increase in the strain and a reduction in crystallite size, which contributes to peak broadening, related to the FWHM of the peaks (Fig. 1b). The insertion of niobium inside the TiO_2 matrix also promotes the inhibition of anatase → rutile phase transition, which explains the smaller crystallite size, since the presence of small TiO_2 nanoparticles increases the average surface energy, stabilizing the anatase phase.

When the niobium concentration reaches 3.0%, there is no increase in the lattice parameters and strain values. This can be explained by the fact that, when the niobium content increases, there is a strong competition between the atoms of Nb^{5+} and Ti^{4+}, promoting a smaller increase in the parameters, suggesting the beginning of segregation. The concentration of niobium doping around 6.0% causes the segregation of phases, whose niobium oxide in separate phase can be observed with instruments [36].

Since Ti and Nb atoms are in a special position inside the crystal structure, there is no changes in the atomic coordinates, however, there is changes in the position and occupancy of oxygen atom, as seen in Table 2. These changes are caused due to the strain in the crystal and an oxygen-rich environment (TiO_x, $x > 2$), promoting distortions and changes in the atomic positions, bonding lengths and bond angles. The Nb occupancy, obtained by Rietveld refinement, showed good coherence between experimental and theoretical Nb fraction in atomic sites, yielding an occupancy of 0, 0.48, 0.88 and 3.02% for pure TiO_2, 0.5%, 1.0% and 3.0% Nb/TiO_2, respectively.

HRTEM analyses were performed using pure TiO_2 and 3.0% Nb/TiO_2 thin films, calcinated at 500 °C. Figure 3a shows pure the TiO_2 thin film, which can be described as a polycrystalline material, showing several diffraction contrasts and an interconnected nanoparticles. Figure 3b represents a magnification of Fig. 3a, showing the diffraction pattern of the TiO_2 anatase, which provided a "d" spacing of 0.342 nm, corroborating XRD results and according to the literature [16].

The insertion of niobium atoms inside the TiO_2 matrix did not change the morphology of the nanoparticles, as seen in Fig. 4a. EDS analysis (Fig. 4b) shows the presence of niobium by the $L\alpha_1$ (2.166 keV) and $L\beta_2$ (2.26 keV) emission lines. The Ka_1 (4.512 keV), $K\beta_1$ (4.933 keV), *La* (0.452 keV) and *Lβ* (0.458 keV) emission lines of titanium were also evidenced. The emission line of copper *La* (0.928 keV) is due to the sample holder grid. The Si and Ca emission lines observed at *Ka* (1.75 keV) and *Ka* (1.75 keV), respectively, are due to the part of the glass substrate that remained attached to the film during the analysis. In the magnifications of Fig. 4c, d, the presence

Table 1 Statistical correlation of the analyzed thin films

Sample	χ^2	R_p (%)	R_{wp} (%)	R_F (%)
TiO_2	1.258	11.20	15.70	8.95
0.5% Nb/TiO_2	1.341	8.97	12.60	8.32
1.0% Nb/TiO_2	1.051	7.78	10.66	7.80
3.0% Nb/TiO_2	1.219	8.21	11.13	8.13

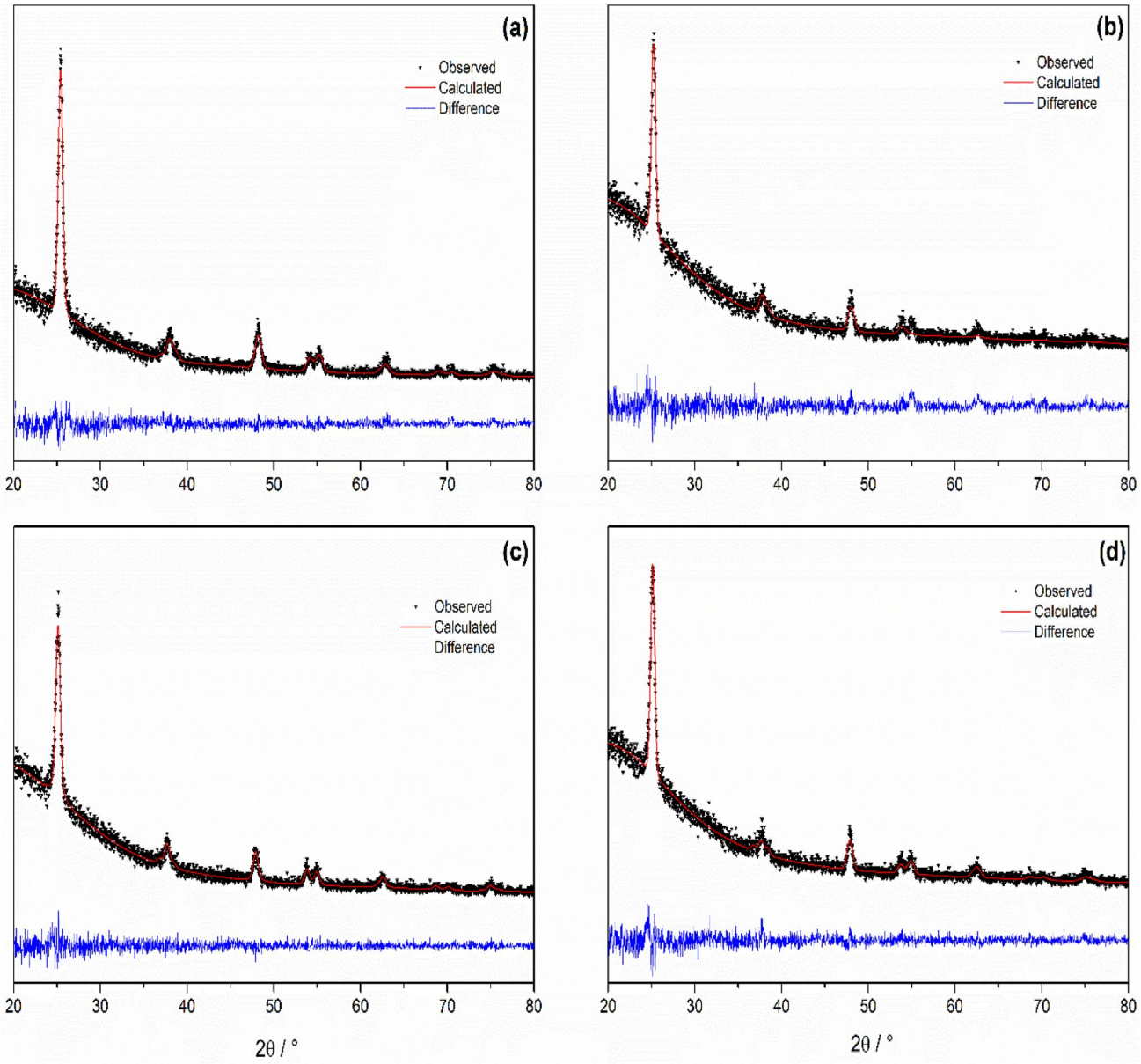

Fig. 2 Rietveld refinement graphs for **a** TiO_2 **b** 0.5% **c** 1.0% and **d** 3.0% Nb/TiO_2 calcined at 500 °C

of round shaped particles was verified, with a more likely random growth, where there is a preferential orientation of (101) anatase crystalline plan, with an interplanar distance of 0.355 nm, corroborating XRD analysis.

The average particle size of pure TiO_2 is (11 ± 1) nm and of the 3.0% Nb/TiO_2 is (6 ± 1) nm, corroborating the crystallite size obtained in Rietveld analysis, showing that there is also a decrease in the average particle size that forms the doped thin film.

AFM analyses were also performed with TiO_2, 0.5, 1.0 and 3.0% Nb/TiO_2 thin films, calcinated at 500 °C. The 3D AFM images are shown in Fig. 5.

The insertion of niobium into the TiO_2 matrix also changed the texture and morphology of the thin film on a micrometer scale, showing a thin film with lower particle size and roughness in comparison with the pure TiO_2. With the addition of 0.5% niobium inside the titanium dioxide matrix, as seen in Fig. 5a, there is a decreasing in the particle size, with a decrease in the average roughness (RMS). An increase in the niobium content (1.0%) also changed the morphology, diminishing the particle size and the RMS value, indicating that the niobium is responsible for the changes in the morphology of the thin films. This can be attributed to the substitutional effect of Nb^{5+} at some

Table 2 Obtained crystallographic data from Rietveld analysis

Sample	$A = b$/Å	c/Å	Volume/Å^3	Average Strain/%	Average crystallite size/nm	Atomic Coordinates (x, y, z)	Occupancy	Atom
TiO_2	3.7655 (6)	9.4515 (2)	134	0.017	11	0, 0.2500, 0.3750	1.000	Ti
						0, 0.2500, 0.3750	1.000	O
							0.000	Nb
0.5% Nb/ TiO_2	3.7835 (6)	9.5055 (8)	136	0.837	7	0, 0.25, 0.375	0.9940	Ti
						0, 0.25, 0.168	1.0110	O
						0, 0.25, 0.375	0.0048	Nb
1.0% Nb/ TiO_2	3.8102 (7)	9.5656 (5)	139	0.867	5	0, 0.25, 0.375	0.9896	Ti
						0, 0.25, 0.168	1.0096	O
						0, 0.25, 0.375	0.0096	Nb
3.0% Nb/ TiO_2	3.8004 (7)	9.5455 (7)	138	0.781	5	0, 0.25, 0.375	0.9689	Ti
						0, 0.25, 0.169	1.0104	O
						0, 0.25, 0.375	0.0301	Nb

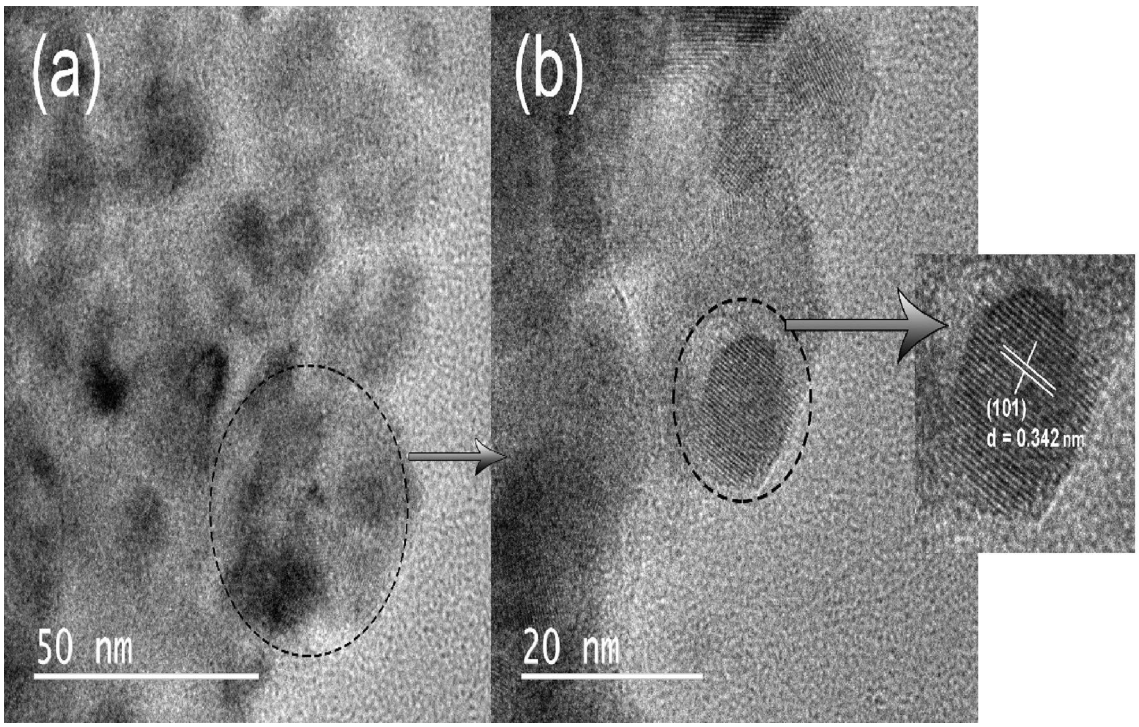

Fig. 3 HRTEM analysis of **a** pure TiO_2 and **b** magnification indicating a presence of a nanocrystal

Ti^{4+} sites facilitated by the use of sol–gel synthesis, which can lead to local charge displacement, with a consequent decreasing in average particle size, corroborating some previous works [5, 37]. An increase in the average particle size and RMS values is observed in thin films of 3.0% of Nb/ TiO_2, which can be attributed to the site competition effect between Ti^{4+} and Nb^{5+} atoms, suggesting a greater surface entropy that leads to a decrease in surface energy due to the formation of larger particles [38].

Table 3 presents values of RMS and mechanical properties of the obtained thin films. The nanohardness of Nb-doped thin films increased in comparison with pure titanium dioxide. This phenomenon can be attributed to a lower particle size and roughness, since films with lower roughness presents greater resistance to nucleation and extension of microcracks, resulting in larger rigidity, strength and toughness according to the theory of mechanical fractures.

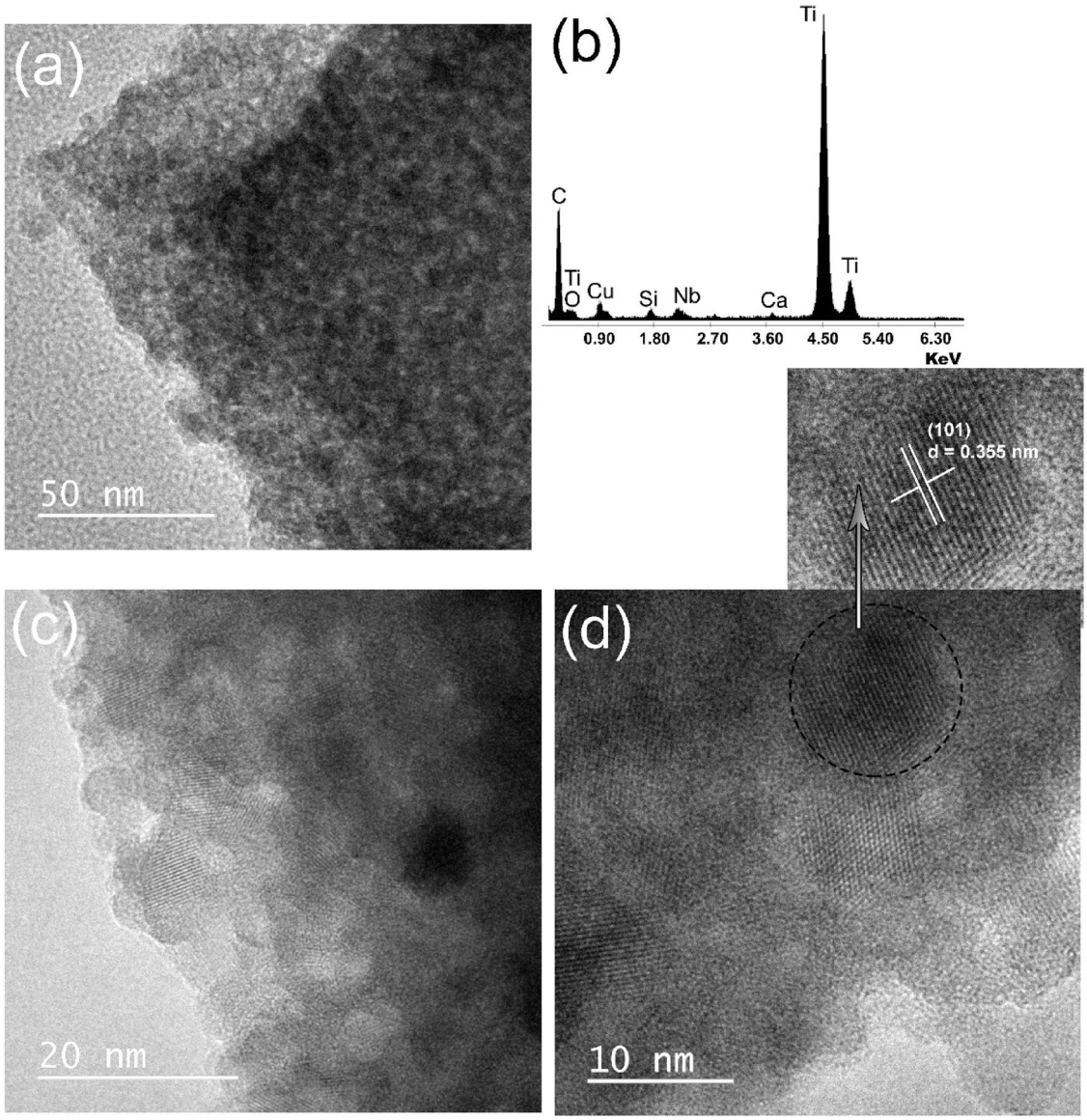

Fig. 4 **a** HRTEM analysis of 3.0% Nb/TiO2, **b** EDS analysis and **c** magnification of the sample, showing **d** diffraction patterns in the nanoparticles

3.2 Optical evaluation and properties of thin films

All studied thin films presented a good optical aspect, without cracks and good adhesion on the glass substrate. Those characteristics are crucial for a good optical study of the samples, which was performed using the transmittance curves to understand the optical behavior of the films in the UV–Visible region. Figure 6 presents the transmittance curves of the thin films calcinated at 500 °C.

Figure 6 shows that the undoped film presents one interference fringe and two for the doped thin films. This occurs due to the difference in the thickness and refractive index of thin films, as discussed by Israelachvili et al. [39]. Another point to account is the difference in the absorption region of the thin films, leading to consider that there are changes in the absorption coefficient and the bandgap values (Table 4).

A method described by Swanepoel [40] was applied to determine the absorption coefficients of the thin films from transmittance data using the refractive index (n) and thickness (d) obtained by SE. Then, the traditional Tauc method [33] is applied to obtain the bandgap values. As all thin films crystallized in the anatase phase of titanium dioxide, the samples were treated to obtain the indirect value of the most characteristic and important bandgap for this phase (Table 4).

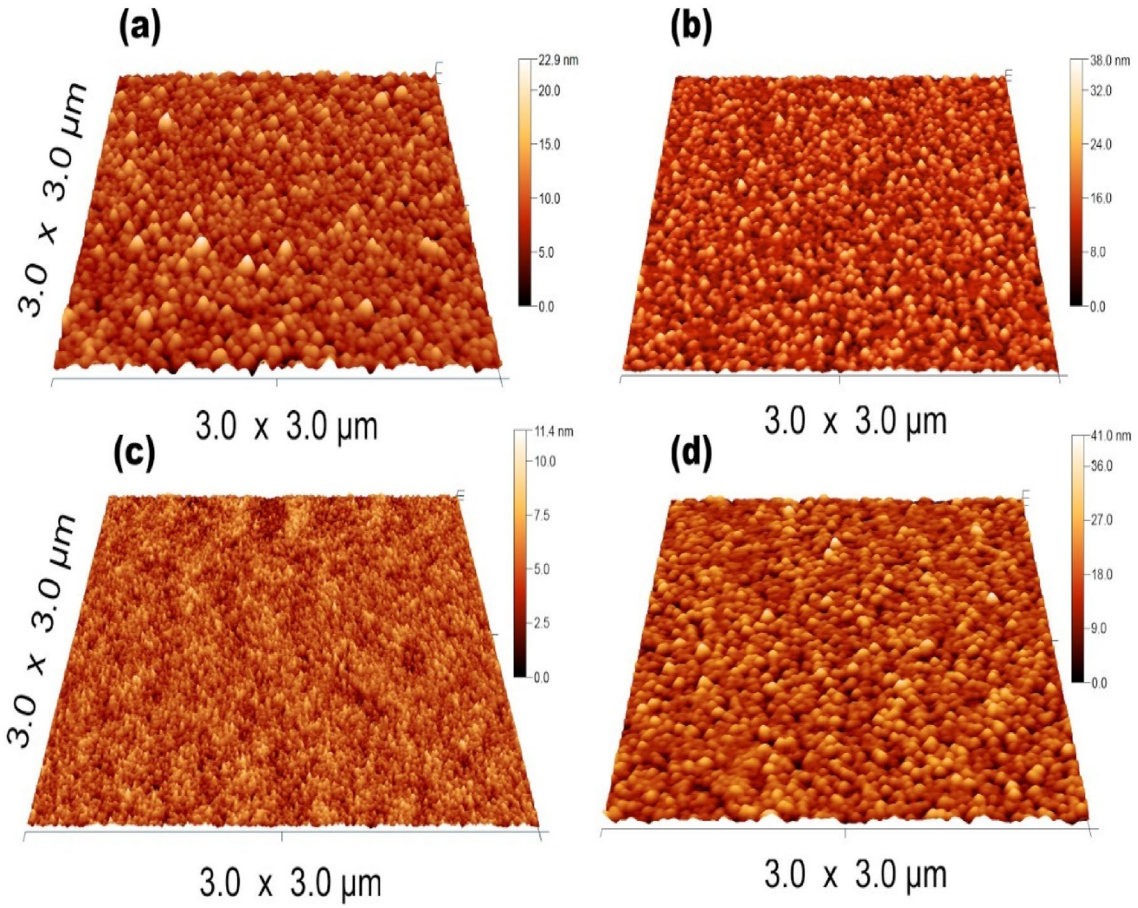

Fig. 5 AFM analysis of **a** TiO_2 **b** 0.5%Nb/TiO_2 **c** 1.0%Nb/TiO_2 and **d** 3.0%Nb/TiO_2 calcined at 500 °C—3D vision at 3×3 µm

Table 3 Mechanical properties of the thin films

Film	RMS roughness/nm	Nanohardness/GPa	Young's modulus/GPa	Maximum depth/nm
TiO2	3.3 ± 0.1	(3.8 ± 0.5)	(44.4 ± 3.1)	(109 ± 6)
0.5% Nb/TiO2	1.7 ± 0.2	(4.5 ± 0.7)	(44.6 ± 4.1)	(104 ± 7)
1.0% Nb/TiO2	0.84 ± 0.08	(4.1 ± 0.2)	(37.0 ± 1.7)	(111 ± 2)
3.0% Nb/TiO2	2.2 ± 0.1	(4.5 ± 0.9)	(51.8 ± 13.9)	(101 ± 9)

The bandgap values obtained from the two techniques are consistent with values in the literature [41], which showed changes between doped and doped thin films, mainly for samples calcined at 500 °C. The formation of the anatase phase occurs around this temperature, promoting changes in energy levels due to changes in the crystal structure, as reported in some experimental and theoretical studies [42, 43], where the insertion of niobium slightly alters the energies of the valence and conduction band. The variation between the values obtained by the two techniques for the thin films calcined at 400 °C is greater and can be explained by the fact that at this temperature the anatase phase is not yet formed and the material is still porous, a fact that is not contemplated by the model used in the ellipsometric analysis [40].

Spectroscopic ellipsometry (SE) was applied to understand the changes in the dielectric function (ε) varying the temperature (400 and 500 °C) and the amount of niobium (0, 0.5, 1.0 and 3.0% in molar ratio). The dielectric function is described as $\varepsilon = \varepsilon_1 - i\varepsilon_2$, where ε is the complex dielectric function, ε_1 is the real part and ε_2 is the imaginary part. The ε_1 and ε_2 are correlated to the refractive index (n) and the extinction coefficient (k), $\varepsilon_1 = n^2 - k^2$ and $\varepsilon_2 = 2kn$.

For the optical characterization, Psi (Ψ) and Delta (Δ) curves of the substrate and the thin films were obtained. A Cauchy model was used to describe the optical data for the

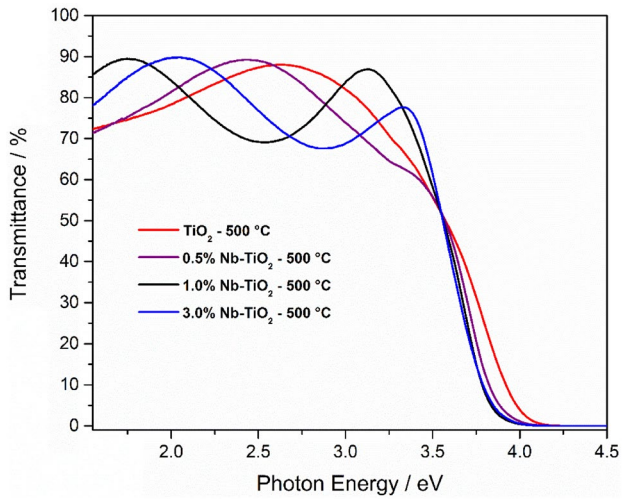

Fig. 6 Transmittance spectra of thin films calcinated at 500 °C

Table 4 Bandgap values using Tauc and ellipsometry methods of the thin films calcined at 400 and 500 °C

Sample	Bandgap (Tauc)/eV	Bandgap (Ellipsometry)/eV
TiO_2—400 °C	3.51 (5)	3.49 (9)
0.5% Nb/TiO_2—400 °C	3.48 (7)	3.37 (1)
1.0% Nb/TiO_2—400 °C	3.51 (5)	3.34 (1)
3.0% Nb/TiO_2—400 °C	3.50 (5)	3.37 (3)
TiO_2—500 °C	3.41 (5)	3.43 (9)
0.5% Nb/TiO_2—500 °C	3.31 (3)	3.29 (7)
1.0% Nb/TiO_2—500 °C	3.28 (4)	3.24 (8)
3.0% Nb/TiO_2—500 °C	3.29 (1)	3.25 (8)

substrate (glass slide). The model consists of a mathematical power series function, where the refractive index (n) has an indirect relation with the wavelength, and the extinction coefficient (k) is equal to zero. In other words, there is no light absorption. Cauchy model is described below:

$$n(\lambda) = B + \frac{C}{\lambda^2} + \frac{D}{\lambda^4} + \ldots \tag{3}$$

To determine the optical properties of thin films, a Tauc–Lorentz model was used, which is a consistent Kramers–Kronig analytical function where a Lorentz oscillator is coupled with a Tauc function to describe the light absorption around the bandgap value, with no absorption below this value ($\varepsilon_2 = 0$; $E < E_g$). The imaginary part of the dielectric function is given by:

$$\varepsilon_2 = \frac{\mathrm{AEn}_0 C\left(\mathrm{En} - E_g\right)^2}{\left(\mathrm{En}^2 - \mathrm{En}_0^2\right)^2 + C^2\mathrm{En}^2} \frac{1}{\mathrm{En}} \quad (\mathrm{En} > E_g) \tag{4}$$

$$\varepsilon_2 = 0 \quad \left(\mathrm{En} \le E_g\right) \tag{5}$$

where A and C are constants in eV, En is the photon energy and Eg is the bandgap. Some parameters in the Tauc–Lorentz modeling were kept fixed to obtain a more reliable analysis; where $\varepsilon_{\mathrm{inf}} = 1$ is the dielectric function at an infinite frequency, the UV pole amplitude was defined as 8 eV that is an energy range greater than the bandgap, and the infrared pole amplitude (IR pole amp) is equal to 0, since no absorption is expected in the IR region. All other parameters were fitted to achieve the minimum mean squared error (MSE), and all analysis parameters exhibited consistent physical meaning, like $E_o > E_g$ and $\mathrm{Br}_1 < \mathrm{E_g}$, where E_o is the central energy of the oscillator, E_g is the optical bandgap and Br_1 is a damping coefficient linked to the full width at maximum half (FWHM). Table 5 shows the thin film parameters obtained by SE.

MSE is the mean square error, a statistical parameter in SE that shows how close a model is from the experimental values of Psi and Delta, described in the equation $\mathrm{MSE} = \frac{1}{n}\sum_{i=1}^{n}(y_i - \hat{y}_i)^2$, where n is the data point numbers, y_i is the value from the experiment and $\hat{y}_i$ is from the model. MSE values between 1 and 10 can demonstrate a satisfactory analysis. MSE values showed that the analyses were reliable, since the MSE values for 1.0%Nb/TiO_2 samples were < 8

Table 5 Obtained parameters with ellipsometry data

Sample	Thickness/nm	Bandgap/eV	MSE	ε_1/at 1.96 eV	Average porosity/%
TiO_2—400 °C	115	3.52 (1)	4.607	4.296 (2)	18
TiO_2—500 °C	109	3.35 (1)	6.575	4.481 (5)	15
0.5%Nb/TiO_2—400 °C	120	3.45 (9)	4.518	4.854 (0)	12
0.5%Nb/TiO_2—500 °C	119	3.41 (2)	4.599	5.103 (7)	9
1.0%Nb/TiO_2—400 °C	154	3.34 (1)	7.699	5.148 (2)	9
1.0%Nb/TiO_2—500 °C	143	3.24 (8)	7.325	5.296 (2)	7
3.0%Nb/TiO_2—400 °C	138	3.44 (9)	3.942	4.774 (0)	12
3.0%Nb/TiO_2—500 °C	133	3.31 (9)	3.180	4.829 (5)	11

and the other samples showed MSE < 5. Average porosity (P) measurements were performed using the well-known Lorentz–Lorenz equation:

$$P = 1 - \frac{\left(\frac{n_{\text{porous}}^2 - 1}{n_{\text{porous}}^2 + 2}\right)}{\left(\frac{n_{\text{dense}}^2 - 1}{n_{\text{dense}}^2 + 2}\right)} \quad (6)$$

where n_{dense} is the refractive index of a dense TiO_2 film (at 1.96 eV, $n_{\text{dense}} = 2.50$) and n_{porous} is the refractive index of the analyzed thin film. However, it is important to note that the calculated average porosity is an approximation.

All thin films exhibited a reduction in the thickness and the average porosity with the increase in temperature due to the densification process and pore shrinking, corroborating the obtained reflectance data. Average porosity values are also corroborated by AFM analysis, where the pure TiO_2 thin film presents (Fig. 5) more pores than the doped samples. The 1.0%Nb/TiO_2 film shows small number of pores (Fig. 5c) due to the smaller average particle size and due to the higher surface energy presents a tendency to agglomeration and closing in the pores.

The dielectric functions (real and imaginary parts) are shown in Fig. 7. In the visible region there is no light absorption by the thin films, i.e., $\varepsilon_2 = 0$, so the dielectric function can be described as $\varepsilon = n^2$, where n is the refractive index of the material. The TiO_2 thin film showed to be the least dense than other ones, since its ε_1 is lower for this material, which corroborates the obtained average porosity. This phenomenon shows that even a small amount of niobium can cause optical changes: for example, in Fig. 7b, ε_2 values of doped thin films are higher than the values of the pure TiO_2 in the absorption region. Since ε_2 has direct dependence on k (extinction coefficient), it can be related to the absorption coefficient, showing that the insertion of niobium atoms inside the matrix causes an increase in the absorption coefficient.

The niobium atoms have a higher electronic density, strengthening the atomic bond and increasing the density of the states [15], which can cause the densification of the films and, thereby, improve the absorption of light. The significant changes in the dielectric function of the doped thin films are attributed to changes in the crystalline and electronic structure of the material, as well as the surface morphology. The AFM analysis showed differences in average particle size and agglomeration behavior, producing changes in surface roughness and porosity, which directly influence optical properties, since light strongly interacts with the thin film surface. The porosity in the doped thin films also presented a gradient described by the Lorentz–Lorenz equation, where the thin film showed greater porosity in its upper region, corroborating its optical behavior.

The small addition of niobium (0.5%) significantly altered the optical properties of the films, increasing the values of the dielectric constants and changing their bandgap values. However, the addition of 1.0% niobium caused a more significant change in the optical properties of the thin films, with a higher dielectric constant value and smaller bandgap. The films presented smaller particles and lower average porosity. The 3.0%Nb/TiO_2 thin films showed a smaller dielectric constant value than 0.5%Nb/TiO_2, which can be clarified by the fact that with high content of niobium inside the TiO_2 matrix, some atomic site competition takes place in the crystalline system, and part of the niobium atoms can be segregated, causing distortions [17]. Some studies showed that there is an optimal doping concentration for niobium in TiO_2 [17].

3.3 Photocatalytic tests

The photocatalytic activity was carried out, using methylene blue as a pollutant dye model, for pure TiO_2 and 1% Nb/TiO_2 thin films calcinated at 500 °C, which showed the best preliminary results.

Figure 8a shows the decrease in the concentration of methylene blue against the time for the glass substrate (blank sample), TiO_2 and 1%Nb/TiO_2 thin films, showing that a photolysis phenomenon occurs, causing an average of 8% on methylene blue degradation for the glass substrate. However, the thin films presented enhanced activity, 26% and 44% of degradation for pure TiO_2 and 1%Nb/TiO_2, respectively. Previous studies showed different results, as Yin et al. [20] that discussed the fact that Nb-doped TiO_2 thin films showed lower photocatalytic activity, justified by the presence of oxygen and cation vacancies. However, in this work, the XRD with Rietveld refinement analysis showed a thin film with an excess of oxygen. Other studies demonstrate that Nb-doped TiO_2 has higher activity, as Lee et al. [17] that obtained a degradation of 21% using a 9%Nb/TiO_2 photocatalyst and 11% for pure TiO_2. In our work, a degradation of 44% was also obtained with a lower concentration of niobium (Nb/Ti = 1%), indicating that other factors can affect the activity of the material, such as edge and intensity of light absorption, roughness, morphology and crystalline structure.

The presented results indicate that the Nb-doped TiO_2 thin films have higher activity due to an increase in the numbers of electron–hole pairs [44, 45], caused by the insertion of Nb^{5+}, which can be attributed to a higher value of dielectric constant. The increase in the oxygen content presented in Table 2 also plays an important role, promoting a negatively charged surface, and since MB is a cationic dye, the interaction between the pollutant and the surface is more favorable than the pure TiO_2 film. The thin film morphology also plays an important role, since AFM analysis showed that 1%Nb/TiO_2 thin film

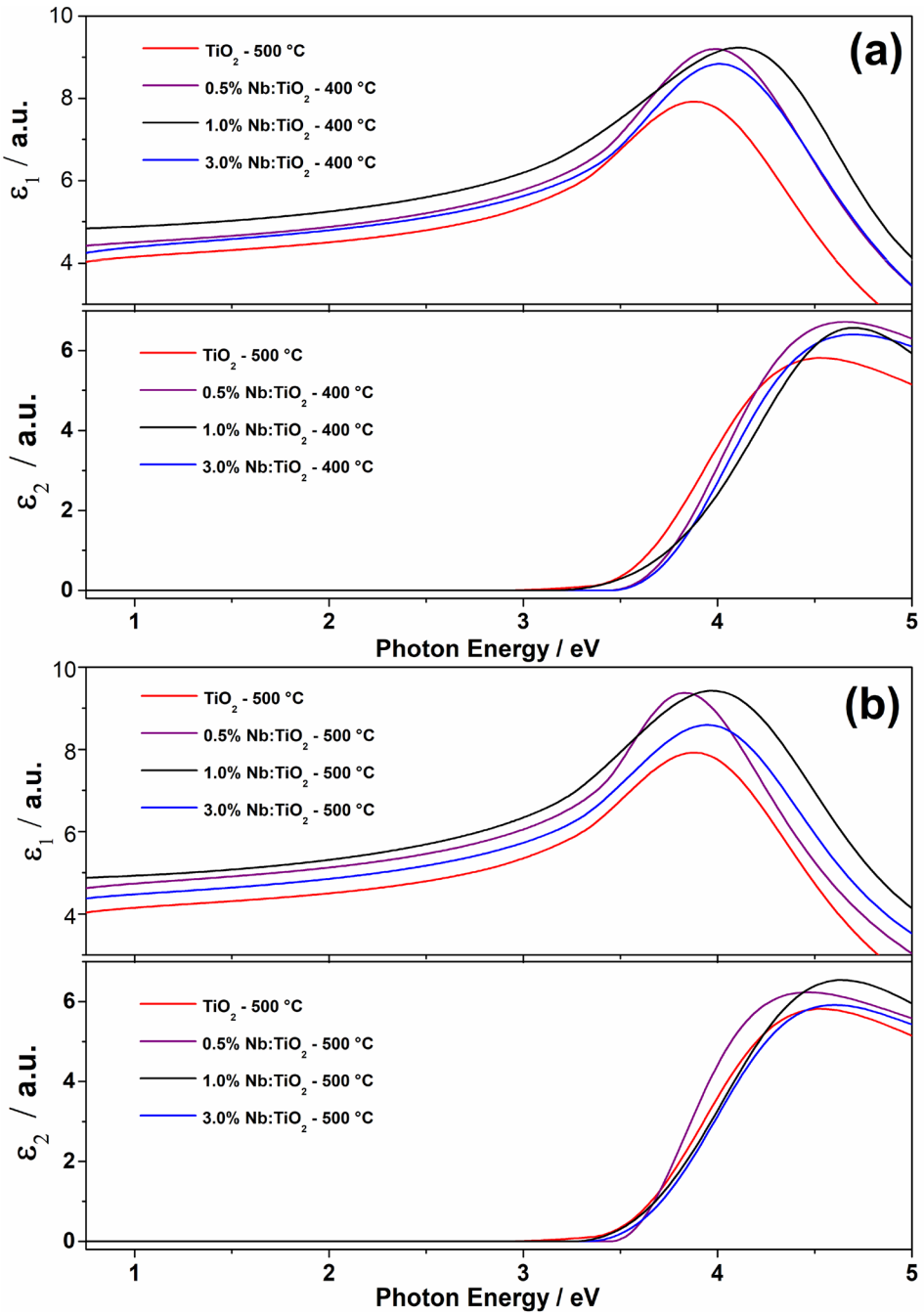

Fig. 7 Real and Imaginary dielectric function for Nb/TiO_2 thin films calcinated at **a** 400 °C and **b** 500 °C (TiO_2 calcined at 500 °C was used for comparison)

presents lower roughness and smaller particle size, which could increase the surface energy in the sample, leading to a higher adsorption of methylene blue molecules on the surface.

Figure 8b presents the degradation kinetics of methylene blue by TiO_2 and 1%Nb/TiO_2 thin films, which can be analyzed using a pseudo-first-order kinetic model.

$$\ln\left(\frac{C}{C_0}\right) = -kt \tag{7}$$

The photodegradation of methylene blue follows the Langmuir–Hinshelwood model, in which $\ln(C/C_0)$ correlates linearly with the irradiation time (t), where the slope of the curve represents the negative value of the pseudo-first-order rate constant k (min^{-1}) and the intercept is the initial concentration of methylene blue.

Table 6 presents the results of both thin films, showing that the degradation rate of 1%Nb/TiO_2 is almost two times faster than pure TiO_2 thin film. This enhancement in photocatalytic activity for Nb-doped TiO_2 materials was supported by several works, also reported in Table 6. Safiay

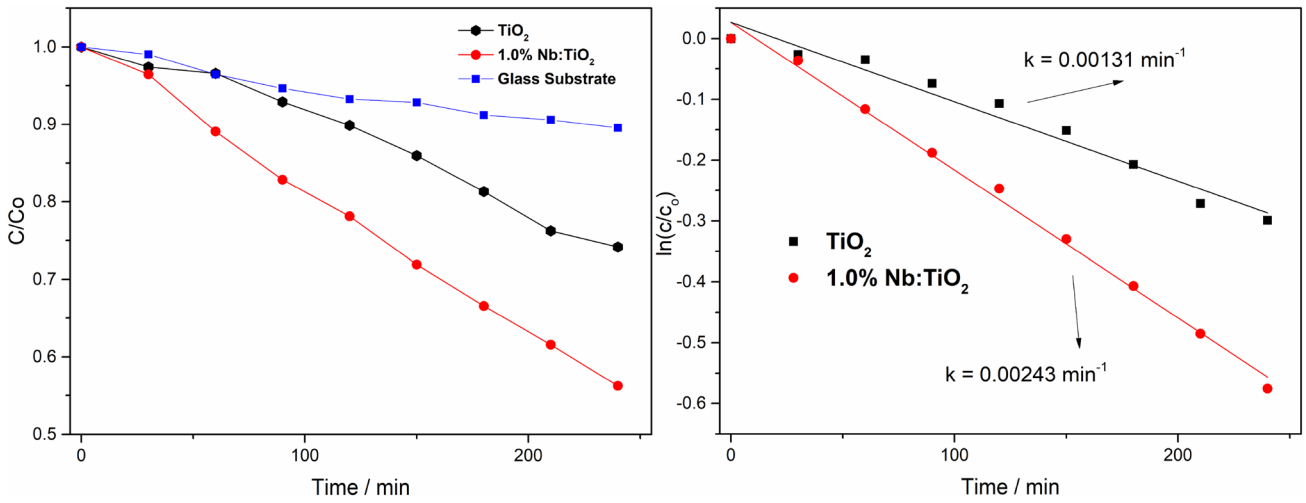

Fig. 8 **a** Reduction of methylene blue concentration and **b** linearization of the concentration curve using first order kinetics

Table 6 Results from pseudo-first-order kinetics of methylene blue degradation by the thin films. Comparison with some literature data."

Sample	Method	k/min^{-1}	Light source	$t_{1/2}$/min	R^2	Reference
TiO_2 (A)	Sol–gel	0.00131	UVC	529	0.98765	This work
1%Nb/TiO_2 (A)	Sol–gel	0.00243	UVC	285	0.99426	This work
TiO_2 (A)	Sol–gel	0.00107	UVA	648	–	[17]
9%Nb-TiO_2 (A)	Sol–gel	0.00212	UVA	326	–	
59%Nb/TiO_2 (R)	Sol–gel	0.00497	UVA	139	–	[17]
3%Nb/TiO_2 (Am)	Sol–gel	0.00010	UV	6931	0.95	[44]
2%Nb/TiO_2 (A)[a]	$TiCl_4$	0.00010	Xe lamp	6931	–	[45]
1%Nb/TiO_2 (A)	Sol–gel	0.00680	Halogen	102	0.7782	[46]

A = Anatase, R = rutile and Am = amorphous

[a]Synthesized microspheres

et al. [46] presented a high degradation ratio of MB with a 1.0% Nb-doped TiO_2 thin film; however, they used a halogen lamp and their linear regression presented low R^2 values, indicating small reliability. To briefly summarize, it is hard to obtain a trustful comparison with the literature on the MB degradation by Nb-doped TiO_2 thin films, since there is a lot of missing information, like lamp luminosity, sample distance and statistical data. However, all presented studies in Table 6 obtained higher MB degradation using the niobium-doped thin films than pure TiO_2 thin films, point out that suitable surface morphology, crystal phase, bandgap values and niobium content plays a crucial role in MB photocatalysis, inciting further studies in photocatalysis applications.

4 Conclusion

The sol–gel synthesis was used to prepare Nb/TiO_2 thin film free of cracks and with good adhesion on the substrate. Good evaluation of the crystal structure and optical properties of the synthesized pure TiO_2 and Nb-doped TiO_2 thin films was achieved with characterization techniques such as XRD with Rietveld analysis and spectroscopic ellipsometry. The insertion of Nb^{5+} atoms inside the TiO_2 structure, replacing the Ti^{4+} caused distortions in the crystalline structure, such as increased strain and changes in the lattice parameters. The niobium substitutional effect in different amounts changed the morphological and structural characteristics of the thin films, being the sample with 1% Nb/TiO_2 the most distinct, with lower RMS and average particle size, leading to different optical and mechanical properties. The bandgap and the refractive index of the samples changed, showing different porosity for all samples. Despite the lower porosity for the doped thin films, they showed an improvement in the photocatalytic degradation of methylene blue, almost two times higher than the undoped thin films, which can be attributed to the better light absorption (k constant 85% higher than the undoped film), a high number of electron–hole pairs, bandgap changes, higher specific surface area and adequate morphology. These properties make the Nb/TiO_2 thin

films a promising material for environmental and energy applications.

Acknowledgements We are thankful to the funding agencies CAPES, CNPq and FAPEMIG, the Microscopy Center of UFMG for the images and the CBMM by the niobium precursor.

Declarations

Conflict of interest There are no conflicts of interest.

References

1. A.M. Bakhshayesh, N. Bakhshayesh, Improved short-circuit current density of dye-sensitized solar cells aided by Sr, Nb co-doped Ti_O2 spherical particles derived from sol-gel route. J. Sol-Gel Sci. Tech. **77**, 228–239 (2016)
2. N.P. Chadwick, E.N.K. Glover, S. Sathasivam, S.N. Basahel, S.A. Althabaiti, A.O. Alyoubi, I.P. Parkin, C.J. Carmalt, Photo-activity and low resistivity in N/Nb Co-doped TiO_2 thin films by combinatorial AACVD. J. Mater. Chem. A **4**, 407–415 (2016)
3. N.D.S. Mohallem, M.M. Viana, M.A.M.L. de Jesus, G.H.M. Gomes, L.F.S. Lima, E.D.S. Alves, Pure and nanocomposite thin films based on TiO_2 prepared by sol-gel process. Ed BoD, Chapter **4**, 81–99 (2018)
4. A.F.R. Silva, N.D.S. Mohallem, M.M. Viana, Titanium dioxide (TiO_2) and silver/titanium dioxide (Ag/TiO_2) thin films with self-cleaning properties. Adv. Mat. Lett. **8**, 444–448 (2017)
5. M. Duta, S. Simeonov, V. Teodorescu, L. Predoana, S. Preda, M. Nicolescu, A. Marin, D. Spasov, M. Gartner, M. Zaharescu, A. Szekeres, Structural and electrical properties of Nb doped TiO_2 films prepared by the sol-gel layer-by-layer technique. Mater. Res. Bull. **74**, 15–20 (2016)
6. J.S. Ogorevc, E. Tratar-Pirc, L. Matoh, B. Peter, Antibacterial and photodegradative properties of metal doped TiO_2 thin films under visible light. Acta. Chim. Slov. **59**, 264–272 (2012)
7. J. Tian, H. Gao, H. Deng, L. Sun, H. Kong, P. Yang, J. Chu, Structural, magnetic and optical properties of Ni-doped TiO_2 thin films deposited on silicon(100) substrates by sol–gel process. J. Alloy. Compd. **581**, 318–323 (2013)
8. Y. Castro, A. Duran, Ca doping of mesoporous TiO_2 films for enhanced photocatalytic efficiency under solar irradiation. J. Sol-Gel Sci. Techn. **78**, 482–491 (2016)
9. D. Fischer, Influence of substrate temperature and silver-doping on the structural and optical properties of TiO_2 films. Thin Solid Films **598**, 204–213 (2016)
10. F. Bensouici, M. Bououdina, A.A. Dakhel, R. Tala-Ighil, M. Tounane, A. Iratni, T. Souier, S.L.W. Cai, Optical, structural and photocatalysis properties of Cu-doped TiO_2 thin films. Appl. Surf. Sci. **395**, 110–116 (2017)
11. T.-T. Pham, C. Nguyen-Huy, H.-J. Lee, T.-D. Nguyen-Phan, T.H. Son, C.-K. Kim, E.W. Shin, Cu-doped TiO2/reduced graphene oxide thin-film photocatalysts: effect of Cu content upon methylene blue removal in water. Ceram. Int. **41**, 11184–11193 (2015)
12. L. Lin, H. Wang, H. Luo, P. Xu, Enhanced photocatalysis using side-glowing optical fibers coated with Fe-doped TiO_2 nanocomposite thin films. J. Photochem. Photobiol. A **307–308**, 88–98 (2015)
13. M. Fallah, M.-R. Zamani-Meymian, R. Rahimi, M. Rabbani, Effect of annealing treatment on electrical and optical properties of Nb doped TiO_2 thin films as a TCO prepared by sol–gel spin coating method. Appl. Surf. Sci. **316**, 456–462 (2014)
14. J.P. Niemela, Y. Hirose, T. Hasegawa, M. Karppinen, Transition in electron scattering mechanism in atomic layer deposited Nb: TiO_2 thin films. Appl Phys Lett **106**, 042101 (2015)
15. H. Kamisaka, T. Hitosugi, T. Suenaga, T. Hasegawa, K. Yamashita, Density functional theory based first-principle calculation of Nb-doped anatase TiO_2 and its interactions with oxygen vacancies and interstitial oxygen. J Chem Phys **131**, 034702 (2009)
16. T. Potlog, P. Dumitriu, M. Dobromir, A. Manole, D. Luca, Nb-doped TiO_2 thin films for photovoltaic applications. Mater. Design **85**, 558–563 (2015)
17. D.Y. Lee, J.H. Park, Y.H. Kim, M.H. Lee, N.I. Cho, Effect of Nb doping on morphology, crystal structure, optical band gap energy of TiO_2 thin films. Curr. Appl. Phys. **14**, 421–427 (2014)
18. M. Duta, L. Predoana, J.M. Calderon-Moreno, S. Preda, M. Anastasescu, A. Marin, I. Dascalu, P. Chesler, C. Hornoiu, M. Zaharescu, P. Osiceanu, M. Gartner, Nb-doped TiO_2 sol-gel films for CO sensing applications. Mat. Sci. Semicon. Proc. **42**, 397–404 (2016)
19. Y. Lu, S. Khan, C.L. Song, K.K. Wang, G.Z. Yuan, W. Li, G.R. Han, Y. Liu, Doping concentration effects upon column-structured Nb:TiO_2 for transparent conductive thin films prepared by a sol–gel method. J. Alloy. Compd. **663**, 413–418 (2016)
20. M. Yin, X.Z. Liu, L.F. Hu, L. Xu, J. He, Effects of Nb doping on microstructure and photocatalytic properties of TiO_2 thin film. Desalin. Water Treat. **57**, 6910–6915 (2016)
21. Ö.D. Coşkun, S. Demirela, The optical and structural properties of amorphous Nb_2O_5 thin films prepared by RF magnetron sputtering. Appl. Surf. Sci. **277**, 35–39 (2013)
22. A.J. Gardecka, G.K.L. Goh, G. Sankar, I.P. Parkin, On the nature of niobium substitution in niobium doped titania thin films by AACVD and its impact on electrical and optical properties. J. Mater. Chem. A **3**, 17755–17762 (2015)
23. Y. Lu, S. Khan, C.L. Song, K.K. Wang, G.Z. Yuan, W. Li, G.R. Han, Y. Liu, Doping concentration effects upon column-structured Nb:TiO_2 for transparent conductive thin films prepared by a sol-gel method. J. Alloy. Compd. **663**, 413–418 (2016)
24. B.N. Joshi, H. Yoon, M.F.A.M. van Hest, S.S. Yoon, Niobium-doped titania photocatalyst film prepared via a nonaqueous sol-gel method. J. Am. Ceram. Soc. **96**, 2623–2627 (2013)
25. J.M. Liu, X.R. Zhao, L.B. Duan, M.M. Cao, H.N. Sun, J.F. Shao, S.A. Chen, H.Y. Xie, X. Chang, C.L. Chen, Influence of annealing process on conductive properties of Nb-doped TiO_2 polycrystalline films prepared by sol-gel method. Appl. Surf. Sci. **257**, 10156–10160 (2011)
26. J. Krýsa, M. Baudys, M. Zlámal, H. Krýsová, M. Morozová, P. Klusoň, Photocatalytic and photoelectrochemical properties of sol–gel TiO_2 films of controlled thickness and porosity. Catal. Today **230**, 2–7 (2014)
27. M.A.M. Jesus, G.H.M. Gomes, A.S. Ferlauto, L.M. Seara, A.M. Ferreira, N.D.S. Mohallem, A systematic study of multifunctional x TiO2/(100–x)SiO2 thin films prepared by sol–gel process. J. Sol–Gel Sci. Techn. **89**, 380–391 (2018)
28. M. Ramirez-del-Solar, E. Blanco, Porous Thin Films from Sol-Gel, (2017). pp. 157–188
29. A.V. Manole, M. Dobromir, M. Gîrtan, R. Mallet, G. Rusu, D. Luca, Optical properties of Nb-doped TiO_2 thin films prepared by sol–gel method. Ceram. Int. **39**, 4771–4776 (2013)
30. M. Rasheed, R. Barillé, Optical constants of DC sputtering derived ITO, TiO2 and TiO_2: Nb thin films characterized by spectrophotometry and spectroscopic ellipsometry for optoelectronic devices. J. Non-Cryst. Solids **476**, 1–14 (2017)
31. J. Zita, J. Maixner, J. Krýsa, Multilayer TiO_2/SiO_2 thin sol–gel films: effect of calcination temperature and Na+ diffusion. J. Photochem. Photobiol., A **216**, 194–200 (2010)

32. W.C. Oliver, G.M. Pharr, Measurement of hardness and elastic modulus by instrumented indentation: advances in understanding and refinements to methodology. J. Mater. Res. **19**, 3–20 (2011)
33. J. Tauc, Grigorov.R, A. Vancu, Optical properties and electronic structure of amorphous germanium, J. Phys. Soc. Jpn. S 21 (1966) 123-&
34. H. Fujiwara, *Spectroscopic Ellipsometry: Principles and Applications* (Wiley, England, 2007)
35. B.H. Toby, R factors in rietveld analysis: how good is good enough? Powder Diffr. **21**, 67–70 (2006)
36. V.M. Dyekanyenko, V. V. Vavilova, Investigation of phase equilibria in the niobium-titanium-oxygen system and equilibrium diagram construction., Fazovye Ravnovesiya Met. Splavakh, (1981) 245–251
37. J. Yue, C. Suchomski, P. Voepel, R. Ellinghaus, M. Rohnke, T. Leichtweiss, M.T. Elm, B.M. Smarsly, Mesoporous niobium-doped titanium dioxide films from the assembly of crystalline nanoparticles: study on the relationship between the band structure, conductivity and charge storage mechanism. J. Mater. Chem. A **5**, 1978–1988 (2017)
38. Q. Fu, Y. Xue, Z. Cui, Size- and shape-dependent surface thermodynamic properties of nanocrystals. J. Phys. Chem. Solids **116**, 79–85 (2018)
39. J.N. Israelachvili, Thin films studies using multiple-beam interferometry. J. Coll. Interface Sci. **44**, 260–272 (1973)
40. R. Swanepoel, Determination of the thickness and optical constants of amorphous silicon. J. Phps. E: Sci. Instrum. **16**, 1214–1222 (1983)
41. J. Lim, D. Monllor-Satoca, J.S. Jang, S. Lee, W. Choi, Visible light photocatalysis of fullerol-complexed TiO_2 enhanced by Nb doping. Appl. Catal. B-Environ. **152**, 233–240 (2014)
42. T. Hitosugi, H. Kamisaka, K. Yamashita, H. Nogawa, Y. Furubayashi, S. Nakao, N. Yamada, A. Chikamatsu, H. Kumigashira, M. Oshima, Y. Hirose, T. Shimada, T. Hasegawa, Electronic band structure of transparent conductor: Nb-doped anatase TiO2. Appl. Phys. Exp. **1**, 111203 (2008)
43. N.A. Tsvetkov, L.L. Larina, O. Shevaleevskiy, E.A. Al-Ammar, B.T. Ahn, Design of conduction band structure of TiO2electrode using Nb doping for highly efficient dye-sensitized solar cells. Prog. Photovolt. Res. Appl. **20**, 904–911 (2012)
44. C. Adomnite, S. Tascu, D. Luca, M. Dobromir, M. Girtan, D. Mardare, Nb-doped TiO_2 thin films as photocatalytic materials Bull. Mater. Sci. **38**, 1259–1262 (2015)
45. J. Yang, X. Zhang, C. Wang, P. Sun, L. Wang, B. Xia, Y. Liu, Solar photocatalytic activities of porous Nb-doped TiO_2 microspheres prepared by ultrasonic spray pyrolysis. Solid State Sci. **14**, 139–144 (2012)
46. M. Safiay, Z. Khusaimi, A.M. Asib, R.A. Ran, N.E.A. Azhar, F. Hamzah, M. Rusop, Visible-light photocatalysis using Nb-doped TiO_2 nanoparticles synthesized via facile sol-gel method. IEEE Reg. Symp. Micro Nanoelectron. (RSM) **1**, 57–60 (2019)